EES Catalysis

PAPER

View Article Online
View Journal

Cite this: DOI: 10.1039/d5ey00362h

Spatially extended asymmetry directs electron transfer and modulates water oxidation deprotonation behavior on dual-atom catalysts

Jixuan Yang,†[ab] Yaxin Cheng,†[bc] Hao Ma,†[d] Zirui Wang,[b] Ting Wang[c] and Yuanmiao Sun *[b]

Introducing local coordination asymmetry through heteroatom substitution in homonuclear dual-atom catalysts (DACs) is an effective strategy to modulate the electronic state of metal centers. However, this approach often results in chaotic and unpredictable changes in electron transfer between the metals and coordinating atoms, which limits precise adjustment of the intermediate adsorption. In this study, we propose a spatially extended asymmetric coordination design strategy that enables simultaneous and precise regulation of electron transfer and differentiation of metal electronic states. Based on first-principles calculations, the constructed homonuclear DACs embedded in a hexagonal boron nitride/graphene (h-BN/Gra) heterostructure demonstrate well-defined electron transfer. The electronegativity differences among B, N, and C coordination atoms lead to distinct d-orbital configurations at the metal centers, which in turn modulate the *OH–*OH deprotonation behavior, following the trend of N coordination > C coordination > B coordination. The constructed volcano plot using the descriptor of $\Delta G_{*O-*OH} - \Delta G_{*OH-*OH}$ provides clear theoretical guidance and design principles for optimizing oxygen evolution reaction activity. This work establishes a conceptual transition from local to spatially extended asymmetric coordination, offering a new theoretical framework for the rational design of asymmetric DACs.

Received 25th December 2025,
Accepted 5th March 2026

DOI: 10.1039/d5ey00362h

rsc.li/eescatalysis

Broader context

Developing efficient electrocatalysts is essential for advancing sustainable energy conversion technologies, particularly for water electrolysis, where the oxygen evolution reaction (OER) remains a major kinetic bottleneck. Dual atom catalysts (DACs) have emerged as a promising platform due to the combination of high metal utilization and cooperative catalytic effects. However, the rational design of homonuclear DACs remains challenging. Introducing asymmetry through local coordination engineering, typically *via* heteroatom substitution, often results in poorly controlled electronic structures, which limits the precise optimization of OER activity. This work introduces a spatially extended asymmetric coordination design strategy that represents a conceptual transition beyond local coordination asymmetry. By embedding homonuclear DACs into a heterostructured support with intrinsically distinct coordination environments, this approach enables simultaneous and deterministic regulation of electron transfer and differentiation of metal electronic states. As a result, well-defined relationships between the coordination environment, electronic structure, and OER energetics can be established, providing clear theoretical guidance for catalyst optimization and offering a generalizable framework for the rational design of asymmetric DACs.

Introduction

The oxygen evolution reaction (OER) serves as a central half-reaction in key energy conversion technologies,[1] including water splitting for hydrogen production,[2–4] rechargeable metal–air batteries,[5–7] and CO_2 reduction.[8,9] Efficient implementation of the OER is crucial for renewable energy storage and utilization. However, the inherent four-electron transfer process in the OER exhibits slow kinetics, resulting in high overpotential and large energy consumption.[10–12] Noble metal-based catalysts, such as IrO_2 and RuO_2,[13–16] demonstrate excellent OER catalytic

[a] Southern University of Science and Technology, Shenzhen, Guangdong 518055, China
[b] Institute of Technology for Carbon Neutrality, Shenzhen Institutes of Advanced Technology, Chinese Academy of Sciences, Shenzhen 518055, China. E-mail: sunym@siat.ac.cn
[c] College of the Environment & Ecology, Fujian Key Laboratory of Coastal Pollution Prevention and Control, Xiamen University, Xiamen 361102, P. R. China
[d] School of Information and Electronic Engineering, Shandong Technology and Business University, Yantai 264005, China
† Jixuan Yang, Yaxin Cheng, and Hao Ma contributed equally to this work.

performance, yet their high cost and scarcity hinder large-scale commercial adoption.[17,18] Therefore, developing alternative OER catalysts with high activity and durability remains a critical challenge.

Single-atom catalysts (SACs) possess atomically dispersed metal sites with high atomic utilization efficiency and uniform active centers, exhibiting great potential for the OER.[19,20] However, SACs face two severe drawbacks in electrocatalysis, *i.e.*, adsorption rigidity and intrinsic linear scaling relationships between adsorption energies.[21] The former hinders adjustment of the configuration to accommodate different intermediates while the latter fundamentally restricts catalytic efficiency in reactions involving multiple or complex intermediates.[22] Building on SACs, the introduction of a second metal active site leads to the formation of dual-atom catalysts (DACs). DACs can retain the advantages of SACs as well as enable more flexible regulation of intermediate adsorption through electronic coupling and synergistic interactions between adjacent metal centers,[23] thereby providing more configurational space for adsorption manipulation.[24] In addition, DACs can facilitate the direct coupling of oxygenated intermediates, which helps circumvent the intrinsic linear scaling relationship between *OH and *OOH species.[25] This process can bypass the high-energy *OOH formation step and effectively lower the overall reaction barrier.[26]

Despite these merits, the full potential of DACs remains unexploited, primarily because of their homonuclearity feature, *i.e.*, the nearly identical electronic states of the metal centers under identical coordination environments.[27] This restricts the precise regulation of intermediate adsorption and subtle manipulation of reaction pathways. To overcome this limitation, introducing asymmetry at the homonuclear dual-metal sites has been proposed.[28,29] A simple and experimentally achievable strategy is substituting one of the original coordination atoms (*e.g.*, N) with a heteroatom, such as S, P, or B,[30,31] to break the local symmetry and construct asymmetrically coordinated DACs. The substitution of a coordinating atom can influence the local electron transfer between the metal center and the coordination environment, thereby bringing electronic state differences to the metal centers.

However, the disruption of local symmetry in DACs typically induces chaotic and unpredictable changes in electron transfer between the d-orbitals of metals and the p-orbitals of coordinating atoms, because electrons may redistribute within the local environment. As a result, replacing a single coordinating atom generally cannot allow precise prediction of the electronic states of metal centers, nor can it reliably establish a stable differentiation on the electronic states of metal centers.[32] Meanwhile, such disruption of local symmetry typically can only produce minor differences in the electronic states of the metal centers, making it difficult to adjust the intermediate adsorption across a wider energy range on the dual-metal sites and,[33] therefore, leading to limited manipulation of the reaction activity and selectivity. To address these drawbacks, the design of spatially extended asymmetric coordination of DACs becomes an urgent issue, which can simultaneously achieve precise control of electron transfer and stable electronic state differences, as well as a wide energy range for intermediate adsorption on dual-metal sites.

In this work, we computationally designed and demonstrated a homonuclear DACs system with a spatially extended asymmetric coordination environment, *i.e.*, the hexagonal boron nitride/graphene heterostructure (h-BN/Gra heterostructure). Spatially extended asymmetric coordination refers to a structural motif in which each metal center maintains a uniform local coordination sphere composed of identical coordinating atoms, and the overall asymmetry originates from the spatial differentiation of coordination environments between distinct metal sites. This type of asymmetry is fundamentally different from heteroatom-substitution-induced asymmetry, in which the local replacement of individual coordinating atoms directly breaks the coordination symmetry at a single metal site. The system's stability was confirmed through the verification of its negative formation energy and positive dissolution potential. We systematically investigated how spatially extended asymmetry affects electron transfer, alters the electronic state of metal centers, and influences the OER catalytic performance. We found that differences in electronegativity among the B, N, and C coordinating atoms lead to distinct electronic states at the metal sites. These electronic states can precisely modulate their d-electron configurations, especially influencing the d_{z^2} orbital, and thereby influence the deprotonation of the *OH–*OH intermediate (Fig. 1a). Our results indicate that a more positively charged metal center enhances deprotonation capability, following the trend of N coordination > C coordination > B coordination. Furthermore, during the *OH–*OH deprotonation process, the B-coordinated metal atom cannot effectively stabilize *O, resulting in over-adsorption of *O–*OH. Finally, we identified the *O–*OH intermediate as a key reaction species and $\Delta G_{*O-*OH} - \Delta G_{*OH-*OH}$ as an effective descriptor for overall OER activity. In this work, a transition in coordination design from local to spatially extended asymmetry was achieved. By elucidating the relationship between electron transfer and intermediate adsorption, this study reveals new pathways for holistically modulating catalytic reactions and offers a theoretical framework for the rational design of spatially extended asymmetric coordination systems.

Methods

All DFT calculations are carried out using the projector-augmented wave (PAW) method as implemented in the Vienna *Ab initio* Simulation Package (VASP).[34–36] The exchange–correlation interactions were treated using the Perdew–Burke–Ernzerhof (PBE) functional within the framework of the generalized gradient approximation (GGA).[37] A plane-wave cut-off energy of 450 eV was adopted for the expansion of electronic wave functions. The convergence criteria for the total energy and atomic forces were set to 10^{-5} eV and 0.02 eV $Å^{-1}$, respectively. The long-range van der Waals interactions were corrected using the DFT-D3 method with Becke–Johnson

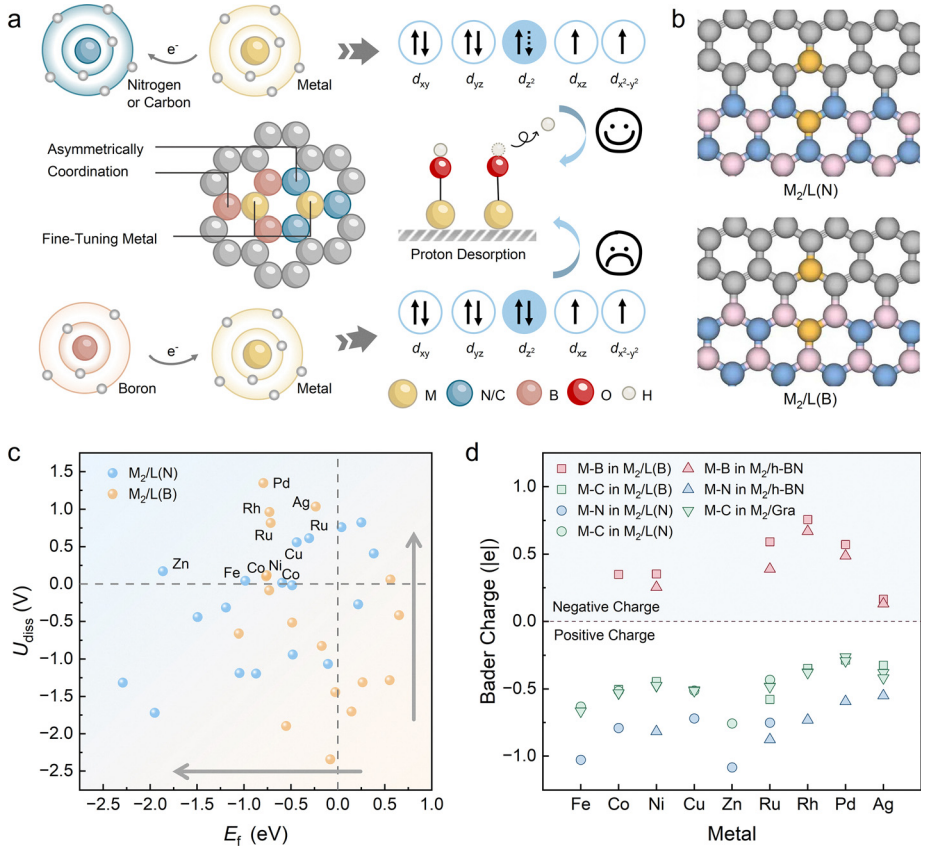

Fig. 1 Asymmetric coordination strategy for OER activities modulation and electronic transfer analysis of DACs. (a) Schematic of asymmetric coordination modulation tuning metal–ligand interactions to regulate *OH proton desorption. (b) Structural prototypes of dual-atom anchored on h-BN/Gra model, where L(N) and L(B) denote heterostructures with N–C and B–C interfacial linkages, respectively. (c) Computed formation energies (E_f) and dissolution potentials (U_{diss}) of M_2/L(N) and M_2/L(B). Here, the direction indicated by the arrow corresponds to greater stability. (d) Bader charge distributions for metal atoms in DACs under different coordination.

damping.[38] To construct the h-BN/Gra heterostructure, 4 × 8 × 1 supercells of graphene (64 atoms) and h-BN (64 atoms) were laterally stacked. Two atoms at the interface of the heterostructure were subsequently removed to generate anchoring sites for two metal atoms. The Brillouin zone was sampled using a 2 × 2 × 1 Monkhorst–Pack *k*-point grid,[39] and a vacuum layer of 15 Å was introduced along the vertical direction to eliminate spurious interactions between periodic images.

The formation energy (E_f) of the DACs is calculated as

$$E_f = (E_{2M/slab} - E_{slab} - 2E_{M(bulk)})/2 \quad (1)$$

where $E_{2M/slab}$ is the total energy of the DACs on the heterostructure, E_{slab} is the energy of the bare heterostructure, and $E_{M(bulk)}$ is the energy of a single metal atom in its most stable bulk phase. A negative E_f indicates that the formation of the dual-atom species is thermodynamically favorable, suppressing metal diffusion and aggregation.

The dissolution potential (U_{diss}) is evaluated as

$$U_{diss} = U^{\circ}_{diss}(\text{metal, bulk}) - E_f/eN_e \quad (2)$$

where $U^{\circ}_{diss}(\text{metal, bulk})$ is the standard dissolution potential of the bulk metal, and N_e is the number of electrons involved in the dissolution process. A positive U_{diss} (>0 V *vs.* SHE) indicates that the metal atoms bind strongly to the substrate, ensuring the stability of the DACs under electrochemical conditions.

The OER can be described as a four-electron transfer process with multiple intermediates. The AEM of OER process in acid media follows:

$$H_2O + * \rightarrow *OH + H^+ + e^- \quad (3)$$

$$*OH \rightarrow *O + H^+ + e^- \quad (4)$$

$$*O + H_2O \rightarrow *OOH + H^+ + e^- \quad (5)$$

$$*OOH \rightarrow * + O_2 + H^+ + e^- \quad (6)$$

Here, *, *OH, *O, and *OOH denote adsorbed active site, absorbed OH, O, and OOH, respectively. The OCM of the OER process in acid media follows:

$$H_2O + * \rightarrow *OH + H^+ + e^- \quad (7)$$

$$*OH + H_2O \rightarrow *OH–*OH + H^+ + e^- \quad (8)$$

$$*OH–*OH + H_2O \rightarrow *O–*OH + H^+ + e^- \quad (9)$$

$$*O–*OH \rightarrow * + O_2 + H^+ + e^- \quad (10)$$

The change of Gibbs free energy (ΔG) for each OER elementary step was evaluated using the computational hydrogen electrode (CHE) model by Nørskov *et al.*[40] The ΔG is given as follows:

$$\Delta G = \Delta E + \Delta E_{ZPE} - T\Delta S + \Delta G_U \quad (11)$$

Here, ΔE represents the reaction energy, while ΔE_{ZPE} and ΔS denote the zero-point energy and entropy differences derived from vibrational frequencies at $T = 298.15$ K. ΔG_U represents the free energy contribution from the applied electrode potential and is expressed as $\Delta G_U = -neU$, where n is the number of transferred ($H^+ + e^-$) pairs and U is the applied potential relative to the standard hydrogen electrode (SHE). The free energy of a ($H^+ + e^-$) pair is equivalent to half of a gaseous H_2 molecule under standard reaction conditions of $U = 0$ V, 1 bar H_2, and pH = 0. Since the energy of the high-spin ground state O_2 molecule is poorly described in DFT calculations, its free energy is instead derived from the energies of H_2O (l) and H_2 (g). The overpotential η for the OER is then calculated using the following equation.

$$\eta = \max\{\Delta G_1, \Delta G_2, \Delta G_3, \Delta G_4\}/e - 1.23\ V \quad (12)$$

where ΔG_1, ΔG_2, ΔG_3, and ΔG_4 represent the reaction free energies in eqn (3)–(6) or eqn (7)–(10), respectively.

The VASPKIT code was used to post-process the results of the VASP calculations.[41] Bader charge analysis was performed to assess charge transfer,[42] and crystal orbital Hamilton population (COHP) analysis was carried out using the LOBSTER package to investigate the bonding characteristics between metal atoms and coordinating atoms.[43]

Results and discussion

Construction of spatially extended asymmetry coordination in dual-atom catalysts

Hexagonal boron nitride/graphene lateral heterostructures are ideal two-dimensional material platforms because of their excellent lattice matching, chemical stability, and interfacial charge modulation ability.[44] Considering these advantages, we selected the h-BN/Gra heterostructure as a demonstrative prototype in this work. The heterostructure was constructed by laterally stacking a $4 \times 8 \times 1$ h-BN layer ($a_{h\text{-}BN} = 10.01$ Å, $b_{h\text{-}BN} = 20.02$ Å) and a $4 \times 8 \times 1$ graphene layer ($a_{Gra} = 9.87$ Å, $b_{Gra} = 19.74$ Å), with a negligible 1.79% lattice mismatch, which satisfies the requirement for lattice compatibility.[45,46] Two connection modes of the h-BN/Gra heterostructure were constructed. One has N–C connections at the interface and is denoted as L(N). The other has B–C connections at the interface and is called L(B) (Fig. S1). Compared with monolayer h-BN and graphene, the h-BN/Gra heterostructure has a lower work function (Fig. S2). Therefore, the constructed heterostructure shows a stronger electron donor capability and electrons can more easily migrate and accumulate at the interface. This favors the anchoring and coupling of metal atoms, which provides a suitable condition for constructing DACs.

Based on the h-BN/Gra model, a series of DACs were systematically constructed using 3d and 4d transition metals. Two loading modes of DACs were constructed on h-BN/Gra, which are denoted as M_2/L(N) and M_2/L(B) (Fig. 1b). In M_2/L(N), one of the dual metal atoms coordinates with three N atoms (M–N) and the other with three C atoms (M–C). In M_2/L(B), one of the dual metal atoms coordinates with three B atoms (M–B) and the other with three C atoms (M–C). As shown in Fig. 1c, the thermodynamic and electrochemical stability of the systems was evaluated by calculating the formation energy (E_f) and dissolution potential (U_{diss} *vs.* SHE). Systems with negative E_f (<0 eV) and positive U_{diss} (>0 V) are considered thermodynamically and electrochemically stable (detailed values of E_f and U_{diss} are given in Table S1, SI). Specifically, the stable systems are located in the upper-left area of the coordinate plane.

As shown, among the screened h-BN/Gra systems, those with metal centers of Fe, Co, Ni, Cu, Zn, Ru, Rh, Pd, and Ag are stable and located in the upper-left area. The stable asymmetric DACs anchored at the N–C interface include Fe_2/L(N), Co_2/L(N), Cu_2/L(N), Zn_2/L(N), and Ru_2/L(N). Meanwhile, Co_2/L(B), Ni_2/L(B), Ru_2/L(B), Rh_2/L(B), Pd_2/L(B), and Ag_2/L(B) are stable asymmetric DACs anchored at the B–C interface. Cohesive energy calculations further confirm their thermodynamic stability (Fig. S3), showing that spatially extended asymmetric coordination can effectively stabilize the dual metal active centers on the h-BN/Gra model. The instability of other systems is due to the limited space at the threefold coordination sites, which cannot accommodate metals with large atomic radii. This causes compressive strain in the metal–ligand bonds and distorts local bond angles, resulting in high lattice mismatch energy and structure instability. For comparison, DACs on h-BN and graphene supports were also constructed and optimized. The two metal atoms in the M_2/h-BN system are coordinated with three N and three B atoms, denoted as M–N and M–B sites, respectively. Stability screening (Fig. S4 and Table S2) reveals five stable asymmetric DACs on h-BN, namely Ni_2/h-BN, Ru_2/h-BN, Rh_2/h-BN, Pd_2/h-BN, and Ag_2/h-BN. In contrast, eight configurations are stable on graphene, including Fe_2/Gra, Co_2/Gra, Ni_2/Gra, Cu_2/Gra, Ru_2/Gra, Rh_2/Gra, Pd_2/Gra, and Ag_2/Gra. All stable systems were used for subsequent electronic structure and catalytic performance calculations.

To gain deeper insight into charge redistribution, Bader charge analysis was further performed to investigate electron transfer in the M_2/L(N) and M_2/L(B) systems. As shown in Fig. 1d, all stable M_2/L(N) and M_2/L(B) systems exhibit clear and consistent electron transfer. The transfer strongly depends on the local coordination environment. In M_2/L(N), both M–N and M–C metal centers are positively charged, wherein the M–N metal center exhibits a higher positive charge. In M_2/L(B), the M–B and M–C metal centers exhibit opposite charge characteristics. The M–B metal center gains electrons, resulting in a negative charge on the metal center. In contrast, the M–C metal center loses electrons and exhibits a positive charge. The same trend is observed for DACs constructed on h-BN and graphene. N atoms (with an electronegativity value of 3.04) and C atoms (with an electronegativity value of 2.55) are highly electronegative and tend to gain electrons. Consequently, in N/C-coordinated systems, the metal sites lose electrons and adopt positive charges. In contrast, the B atom has relatively low

electronegativity (with an electronegativity value of 2.04). Therefore, in these B-coordinated systems, electrons flow from B atoms to the metal, resulting in a negative charge for the metal center. As demonstrated, spatially extended asymmetric coordination drives directional electron transfer between the metal and coordinating atoms. As a result, the dual-metal sites exhibit charge asymmetry, which can significantly affect the adsorption of oxygenated intermediates at the active sites.

*OH deprotonation modulated by spatially extended asymmetric coordination

After analyzing the stability and charge redistribution of the modeled systems, the possible OER mechanisms were then evaluated. Specifically, two OER mechanisms are considered, namely the adsorbate evolution mechanism (AEM) and the O–O coupling mechanism (OCM).[47,48] The AEM proceeds through the $H_2O \rightarrow *OH \rightarrow *O \rightarrow *OOH \rightarrow O_2$ pathway,[49] while OCM proceeds through the $H_2O \rightarrow *OH \rightarrow *OH–*OH \rightarrow *O–*OH \rightarrow O_2$ one (Fig. S5).[26,50] By systematically calculating the adsorption free energy of different oxygenated intermediates (*OH, *O, *OH–*OH, *OOH, and *O–*OH) on the dual-metal sites (Tables S3–S19), we identified both the most stable adsorption configurations and the preferred adsorption site for each oxygenated intermediate in the asymmetric DACs. These results were then used for subsequent selectivity calculations. In general, the competition between *OH deprotonation (*OH → *O) and the second *OH adsorption (*OH → *OH–*OH) can serve as a simple and practical criterion to distinguish the two OER mechanisms. Based on the calculated values of $\Delta G_{*OH-*OH} - \Delta G_{*OH}$ and $\Delta G_{*O} - \Delta G_{*OH}$ (Fig. S6), it can be found that the reactions along the OCM pathway are energetically more favorable for the four studied DACs. We further analyzed the selectivity of the four DACs toward *O and *O–*OH, which can help evaluate the likelihood of intermediate crossovers. As presented in Fig. S6, the results show that a clear preferential stabilization of the *O–*OH intermediate over its *O counterpart on dual-metal sites, which effectively rules out the possibility of a crossover between the AEM and OCM pathways and demonstrates that OCM is the more feasible OER mechanism in these DACs.

Upon confirming the OER mechanism of the constructed DACs, the adsorption behavior of each intermediate was subsequently computed. As shown in Fig. 2a, a pronounced coordination selectivity for the *O–*OH is observed. Specifically, in M_2/L(N), deprotonation occurs preferentially at the M–N site rather than the M–C site. In M_2/L(B), deprotonation favors the M–C site rather than the M–B site. These findings demonstrate that spatially extended asymmetric coordination effectively

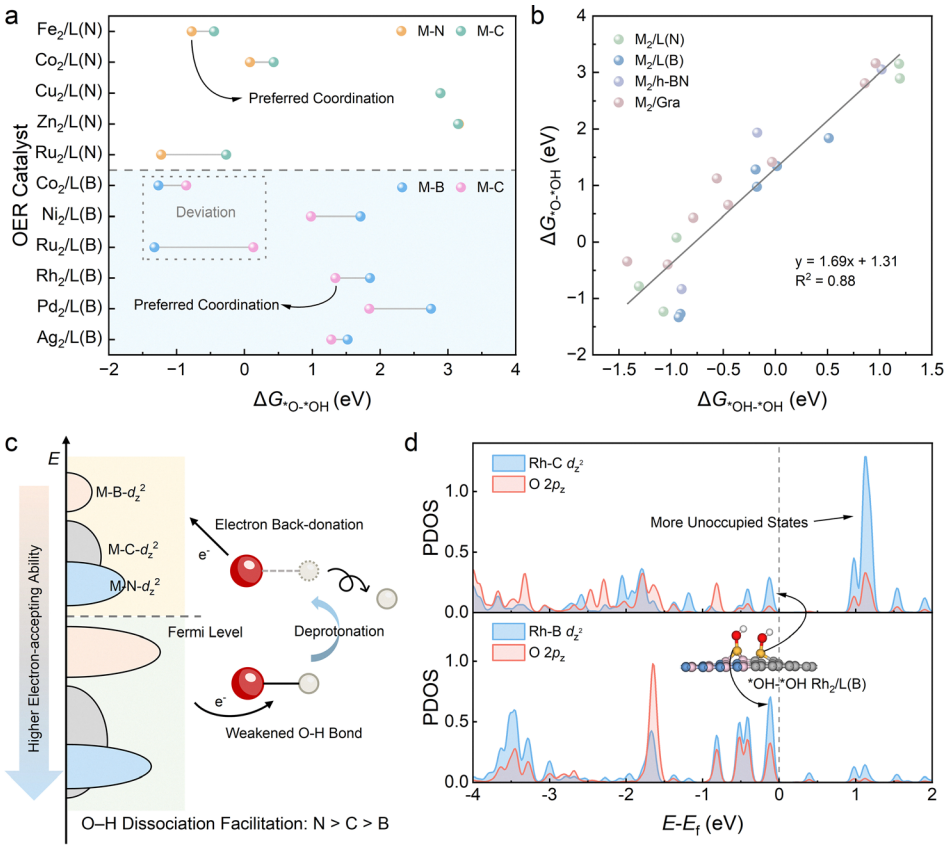

Fig. 2 Asymmetric coordination in DACs modulates *OH deprotonation *via* metal electronic state tuning. (a) Comparison of the deprotonation tendencies of metal sites (M–N, M–C, and M–B) upon *OH adsorption. (b) Linear correlation between the Gibbs free energies of *OH–*OH and *O–*OH intermediates. (c) Schematic illustration of the participation of the metal d_{z^2} orbital in *OH deprotonation under different coordination (B, C, and N). (d) Comparison of the projected density of states (PDOS) of the Rh d_{z^2} and O $2p_z$ orbitals under C and B coordination in Rh_2/L(B).

induces functional differentiation between dual-metal sites. Importantly, the asymmetric coordination in DACs selectively controls the sites where OER deprotonation occurs. To further elucidate the energetic relationships along the reaction pathway, the scaling relationships between intermediate adsorption energies were analyzed. Specifically, the scaling relationship between $\Delta G_{*OH-*OH}$ and ΔG_{*O-*OH} was analyzed (Fig. 2b). As exhibited, a strong linear correlation is obtained (R^2 = 0.88), indicating that both types of intermediates are influenced by similar electronic factors. This means that tuning the coordination atoms can not only affect the thermodynamics of single steps but also regulate the energy distribution across multiple OER steps. The analysis further confirms that the *O–*OH intermediate represents a key step controlling the reaction.

To elucidate the underlying electronic factors, the deprotonation behavior of *OH–*OH at the dual-metal sites was also examined. The key deprotonation of *OH–*OH involves two types of electron rearrangement. First, the d orbitals of the metal tend to overlap with the antibonding orbital of the O–H bond, weakening the O–H bond and facilitating its cleavage.[51] In the adsorption configuration along the z direction, the metal d_z^2 orbital mainly couples with the O $2p_z$ orbital. Through this orbital coupling, electron transfer occurs between the metal center and the O atom, thereby influencing the deprotonation process. Subsequently, following O–H bond cleavage, electron transfer stabilizes the deprotonated product by populating unoccupied metal orbitals from the formed *O.[52,53] Under the regulation of spatially extended asymmetric coordination, the electronic states of the metal exhibit notable differences. Specifically, the M–N and M–C sites are positively charged and possess more unoccupied d-orbitals that can accept feedback electrons from the intermediate, stabilizing the *O species. In contrast, the d orbitals of M–B sites are nearly fully occupied, giving the weakest electron-accepting ability. The limited electron rearrangement at M–B sites restricts O–H bond cleavage. Overall, the O–H bond dissociation ability at the metal active sites follows the trend of N coordination > C coordination > B coordination (Fig. 2c). This indicates that the electronic states of coordination play a decisive role in controlling deprotonation kinetics.

Projected density of states (PDOS) analysis further supports this mechanism. As shown in Fig. 2d, the d_z^2 orbital of the Rh–C site in the Rh_2/L(B) system exhibits more unoccupied states near the Fermi level and strong energy overlap with the O $2p_z$ orbital. This shows a strong electron-accepting capability of the Rh–C site, which facilitates O–H bond cleavage. In the Rh_2/L(B) system, the d_z^2 orbital of the Rh–B site is primarily located below the Fermi level with nearly complete occupancy. It cannot efficiently accept electrons during O–H bond breaking, which impedes the deprotonation process. These observations suggest that, in the B-coordinated system, deprotonation preferentially occurs at the C-coordinated metal site rather than at the B-coordinated site. Consistently, the PDOS of Fe_2/(N), Co_2/(N), and Ni_2/(B), Ru_2/L(N) and Ru_2/L(B) further demonstrates that the deprotonation ability of different coordinating metals follows a trend of N coordination > C coordination > B coordination (Fig. S7–S10). Therefore, by constructing a spatially extended asymmetric coordination environment, the electronic states of the dual-atom active centers can be effectively modulated. This allows precise control over the deprotonation process.

Overstabilized adsorption of *O–*OH on B coordination

In Fig. 2a, the ΔG_{*O-*OH} value on the M–B sites of Co_2/L(B) and Ru_2/L(B) is significantly lower than that on the corresponding M–C sites, indicating stronger *O–*OH adsorption induced by B coordination. A similar trend is also observed in the Ni_2/h-BN and Rh_2/h-BN systems (Table S20). To uncover the origin of the strong *O–*OH adsorption induced by B coordination, the *O–*OH adsorption configurations on metals under different coordination environments (Fig. 3a) were further compared. As illustrated, the M–C sites maintain a conventional M–O bonding configuration (d_{M-O} = 1.68 Å) with moderate adsorption strength. In contrast, on the M–B sites, the *O–*OH intermediate exhibits significantly overstabilized adsorption. The O atom adopts a bridging configuration between the metal atom and the coordinating B atom, forming a co-adsorbed O configuration. Due to the formation of an additional B–O interaction, the M–O bond is elongated (d_{M-O} = 1.90 Å), which causes the O atom to lean toward the B atom. These results indicate that the electron-rich environment of B coordination destabilizes the *O species and promotes bonding between O and the coordinating B atom, which causes the over-adsorption of *O–*OH intermediates. Collectively, this M–O–B co-adsorption configuration explains the lower ΔG_{*O-*OH} observed at the M–B sites of Co_2/L(B), Ru_2/L(B), Ni_2/h-BN, and Rh_2/h-BN.

To examine the bonding interactions between the coordinating atom and O atom, COHP analysis was further conducted (Fig. 3b). In the Ru_2/L(N) system, almost no bonding is observed between the N atom at the Ru–N site and the O atom (ICOHP = −0.15). In contrast, in the Ru_2/L(B) system, a pronounced bonding interaction is found between the B atom at the Ru–B site and the O atom (ICOHP = −5.15). This indicates that the B atom directly participates in bonding with the adsorbed oxygen species, significantly strengthening the overall adsorption and altering the Gibbs free energy of *O–OH. Compared with homonuclear DACs under other coordination environments, the M–B sites in Co_2/L(B), Ru_2/L(B), Ni_2/h-BN, and Rh_2/h-BN exhibit significantly longer O–O distances in the co-adsorption configuration of the *O–*OH intermediate (Fig. 3c). Since O–O coupling requires effective spatial and electronic overlap between the two oxygen atoms, the elongated O–O distance at the M–B sites makes the co-adsorption configuration unfavorable for the subsequent O–O coupling in terms of spatial distance and the lack of orbital overlap.

The molecular orbital (MO) diagram, derived from COHP analysis (Fig. S11), provides further insight into the origin of this coordination-dependent behavior (Fig. 3d). The B atom, with a valence configuration of $2s^2 2p^1$, and the O atom, with $2s^2 2p^4$, form a series of bonding interactions through orbital hybridization. The s, p_z, and p_x orbitals of the B atom form sp^2 hybrid orbitals, while the s and p_z orbitals of O form sp hybrid

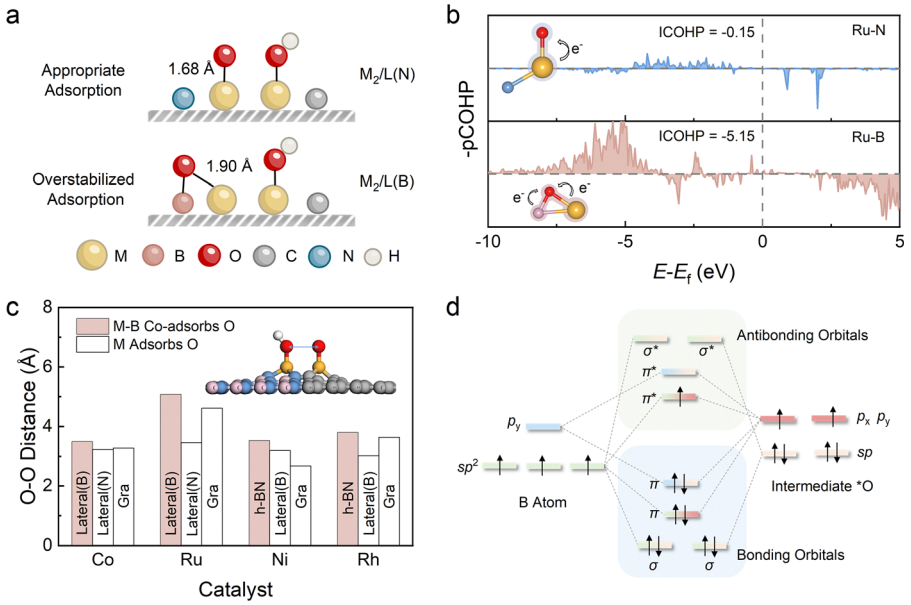

Fig. 3 Electronic origin of the over-stabilized *O–*OH intermediate at the B-coordinated site. (a) Structural comparison of *O–*OH adsorption configurations on M_2/L(N) and M_2/L(B), the latter showing this configuration in only a subset of materials. (b) Comparison of the COHP between N–O and B–O bonds in *O–*OH adsorption on M_2/L(N) and M_2/L(B), respectively. (c) Computed O–O distances in *O–*OH intermediates adsorbed on DACs. (d) Molecular orbital (MO) diagram illustrating the interaction between B atom and intermediate *O.

orbitals (Fig. S12). Two of the sp^2 orbitals of the B atom interact with the two sp orbitals of the O atom, generating a bonding σ MO and an antibonding σ* MO. The remaining sp^2 orbital of the B atom interacts with the p_x orbital of the O atom, producing a low-energy bonding π MO and a corresponding antibonding π* MO. At the same time, the unhybridized p_y orbital of the B atom interacts with one p_y orbital of the O atom, forming a high-energy bonding π MO and antibonding π* MO. All bonding MOs are fully occupied, and one electron occupies an antibonding π* orbital. As the number of p electrons increases, the occupation of antibonding orbitals becomes more pronounced. In contrast, N and C atoms, with valence configurations of $2s^22p^3$ and $2s^22p^2$, respectively, possess more p electrons. When a N or a C atom forms a bond with an O atom, the additional p electrons occupy antibonding orbitals, weakening the N/C–O bonding interaction and suppressing co-adsorption. Consequently, B coordination forms an additional B–O bond that overstabilizes the *O–*OH intermediate and elongates the O–O bond, while N/C coordination maintains conventional M–O adsorption due to the partial occupation of antibonding orbitals.

OER activity influenced by spatially extended asymmetric coordination

As demonstrated above, the OER proceeds *via* the OCM pathway on the constructed DACs. The detailed intermediate evolution of the OCM is illustrated in Fig. 4a. It should be noted that the step of oxygen molecule release, *i.e.*, $*O_2 \rightarrow O_2(g)$, is a non-electrochemical process, and may lead to an overestimation of the overpotential and a misidentification of the potential-determining step (PDS). Therefore, to identify the true rate-determining step (RDS) and rationally assess the catalytic activity, it is important to evaluate the relative magnitude between the O_2 desorption energy and the energy of the PDS (Table S21). The screening of DAC candidates was based on the O_2 desorption energy, with DACs exceeding a defined threshold being eliminated from consideration due to hindered desorption. A comparative analysis of the four studied DACs shows that the h-BN/Gra systems exhibit superior performance, with lower overpotentials and higher theoretical activity limits than the DACs supported solely on h-BN or graphene (Fig. S13).

According to the Sabatier principle, the binding of reaction intermediates to active sites should be neither too strong nor too weak, as either extreme can hinder OER activity. The energy difference $\Delta G_{*O-*OH} - \Delta G_{*OH-*OH}$ was employed as an activity descriptor for the OER performance of these asymmetric DACs. Interestingly, a volcano-shaped relationship with this descriptor is observed for the overpotential (Fig. 4b). As the OER activity of these asymmetric DACs is dominated by the deprotonation of the *OH–*OH intermediate, the energy difference between *O–*OH and *OH–*OH is quantitatively reflected as the thermodynamic energy required for O–H bond dissociation. Therefore, $\Delta G_{*O-*OH} - \Delta G_{*OH-*OH}$ reveals the intrinsic correlation of OER activity under different coordination environments. As exhibited, the M_2/L(N) and M_2/Gra systems are mainly distributed on the right side of the volcano, corresponding to the ''*OH deprotonation-limited'' region. The M_2/L(B) and M_2/h-BN systems lie on the left side, corresponding to the ''O–O coupling-limited'' region. These results indicate that subtle variations of *O–*OH can shift the RDS between deprotonation-limited and coupling-limited regimes, ultimately dictating the overall OER activity.

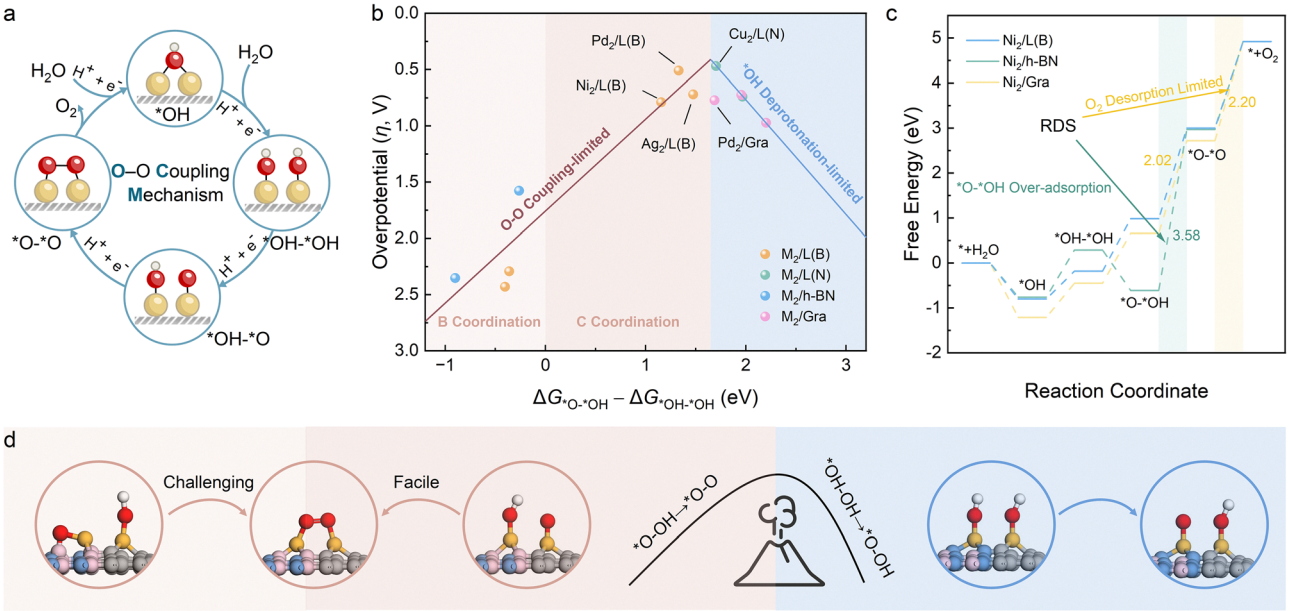

Fig. 4 OER pathways and activity analysis. (a) OER reaction mechanisms following the OCM. (b) Volcano plots of the overpotential *versus* the Gibbs free energy difference between the *O–*OH and *OH–*OH intermediates. (c) OER free-energy diagrams of Ni dual-atom anchored on three different supports. (d) Schematic representation of the factors underlying the volcano-type trend.

To further clarify the reaction characteristics under different supports and coordination environments, we compared the complete OER free-energy pathways of three representative DACs, Ni_2/L(B), Ni_2/h-BN, and Ni_2/Gra, as shown in Fig. 4c. The results show different adsorption of *O–*OH across these systems. In the h-BN system, the *O–*OH intermediate is overstabilized, leading to a significant increase in the energy for O–O coupling. In contrast, the Ni_2/L(B) and Ni_2/Gra systems exhibit moderate *O–*OH binding, allowing the reaction to proceed smoothly along the OCM pathway. It is noteworthy that other asymmetric DACs with similar coordination environments, such as Co_2/L(B) and Ru_2/L(B), show similar reaction trends to Ni_2/L(B). The corresponding free-energy diagrams are presented in Fig. S14. Among these systems, Cu_2/L(N) exhibits the highest catalytic performance. This Gibbs free energy diagram directly correlates the activity distribution observed in the volcano plot with the detailed free-energy pathways, which reveals the correlation between the coordination environment and RDS among different DACs.

As shown in Fig. 4d, the volcano plot trend is elucidated through distinct coordinated structures and distinct adsorption configurations. In the presence of B coordination, *O–*OH adsorption is strong, which results in a lower ΔG_{*O-*OH} and causes more energy to activate the O–O formation step. Particularly, the left side of the volcano plot can be divided into two regions according to the *OH deprotonation metal site, namely deprotonation at the C-coordinated metal site and at the B-coordinated metal site. Deprotonation at the B-coordinated metal site can lead to the formation of a co-adsorption configuration. This results in excessively strong *O–*OH adsorption that places B-coordinated systems in the overly strong-binding region (lower-left corner) of the volcano plot. In contrast, in the absence of B coordination, DACs exhibit a higher ΔG_{*O-*OH}, indicating that the *OH–*OH → *O–*OH deprotonation step becomes the PDS. Therefore, the intrinsic OER activity originates from the precise regulation of *O–*OH adsorption by the spatially extended asymmetric coordination of DACs.

Conclusions

In summary, by using h-BN/Gra heterostructures as prototypes to construct spatially extended asymmetric coordination DACs, we systematically investigated how different coordination environments affect the DAC-catalyzed OER and the underlying mechanisms. Our results indicate significant electron transfer between the coordinating atoms and the metal centers. Specifically, high-electronegativity N/C coordination withdraws electrons from the metal center, yielding a positively charged metal center. In contrast, low-electronegativity B coordination donates electrons to the metals and leads to a negatively charged metal center. This well-defined electron transfer allows precise prediction of the deprotonation sites of the *OH–*OH intermediate, with the deprotonation trend following N coordination > C coordination > B coordination. Moreover, B coordination can lead to bond formation between the O atom and the coordinating B atom, giving rise to M–O–B co-adsorption configurations. These configurations lower ΔG_{*O-*OH}, and due to the increased spatial separation, hinder the O–O coupling step, thereby suppressing the OCM pathway and ultimately reducing the overall OER activity. Finally, activity evaluation shows that DACs constructed on h-BN/Gra exhibit superior performance, with lower overpotentials and higher theoretical activity limits than the DACs supported solely

on h-BN or graphene. Volcano plot analysis further confirms the dominant role of *O–OH in controlling the RDS, highlighting that OER activity primarily arises from the modulation of *O–OH adsorption at the metal sites. This work achieves a transition from locally asymmetric to spatially extended asymmetric coordination design and provides a theoretical framework for the rational design of spatially extended asymmetric coordination systems.

Author contributions

J. Y. conceived and designed the study. Y. S. directed the project. J. Y. conducted the DFT calculations and performed the subsequent data analysis. Y. C. created the graphical figures and illustrations. J. Y. wrote the manuscript. H. M. and Z. W. provided guidance and advice on the manuscript. Y. S. reviewed and edited the manuscript.

Conflicts of interest

There are no conflicts to declare.

Data availability

The data supporting this article have been included as part of the supplementary information (SI). Supplementary information: additional slab models, mechanism diagrams, PDOS diagrams, COHP analyses, and free energies of OER intermediates. See DOI: https://doi.org/10.1039/d5ey00362h.

Acknowledgements

This work is supported by the National Natural Science Foundation of China (52373233 and 52300139). The authors also acknowledge the financial support from the Guangdong Basic and Applied Basic Research Foundation (No. 2024A1515010679) and the Shenzhen Science and Technology Program (KQTD2022 1101093647058).

Notes and references

1 K. Wang, S. Li, J. Li, C. Liang, J. Li, L. Lei, M. Zhu, L. Zhuang, J. Chen, Z. Xu and X. Yao, *Angew. Chem., Int. Ed.*, 2025, **64**, e202511112.
2 D. Guo, Z. Zeng, Z. Wan, Y. Li, B. Xi and C. Wang, *Adv. Funct. Mater.*, 2021, **31**, 2101324.
3 Y. Chang, P. Zhai, J. Hou, J. Zhao and J. Gao, *Adv. Energy Mater.*, 2022, **12**, 2102359.
4 K. Shah, R. Dai, M. Mateen, Z. Hassan, Z. Zhuang, C. Liu, M. Israr, W.-C. Cheong, B. Hu, R. Tu, C. Zhang, X. Chen, Q. Peng, C. Chen and Y. Li, *Angew. Chem., Int. Ed.*, 2022, **61**, e202114951.
5 B. Wei, Z. Fu, D. Legut, T. C. Germann, S. Du, H. Zhang, J. S. Francisco and R. Zhang, *Adv. Mater.*, 2021, **33**, 2102595.
6 D. Ding, K. Shen, X. Chen, H. Chen, J. Chen, T. Fan, R. Wu and Y. Li, *ACS Catal.*, 2018, **8**, 7879–7888.
7 F. N. I. Sari, Y.-C. Lai, Y.-J. Huang, X.-Y. Wei, H. Pourzolfaghar, Y.-H. Chang, M. Ghufron, Y.-Y. Li, Y.-H. Su, O. Clemens and J.-M. Ting, *Adv. Funct. Mater.*, 2024, **34**, 2310181.
8 L. Yu, F. Li, J. Huang, B. G. Sumpter, W. E. Mustain and Z. Chen, *ACS Catal.*, 2023, **13**, 9616–9628.
9 Y. Y. Birdja, E. Pérez-Gallent, M. C. Figueiredo, A. J. Göttle, F. Calle-Vallejo and M. T. M. Koper, *Nat. Energy*, 2019, **4**, 732–745.
10 H. Li, Y. Lin, J. Duan, Q. Wen, Y. Liu and T. Zhai, *Chem. Soc. Rev.*, 2024, **53**, 10709–10740.
11 Y. Chen, J. Meng, M. Xu, L. Qiao, D. Liu, Y. Kong, X. Hu, Q. Liu, M. Chen, S. Lyu, R. Tong and H. Pan, *Adv. Funct. Mater.*, 2025, **35**, 2413474.
12 X. Li, J. Wang, H. Xue, L. Zhao, J. Lu, H. Zhang, M. Yan, F. Deng and C. Hu, *Adv. Funct. Mater.*, 2025, **35**, 2503360.
13 G. Buvat, M. J. Eslamibidgoli, A. H. Youssef, S. Garbarino, A. Ruediger, M. Eikerling and D. Guay, *ACS Catal.*, 2020, **10**, 806–817.
14 B. Liu, Y. Zhao, Y. Wu, Y. Wen, Z. Liu, P. Wang, J. Shu and T. Yi, *Catal. Rev.*, 2025, 1–46.
15 Z. Jiang, L. Shao, Y. Sun, Y. Dong, X. Zheng, T. Wang, J. Li, H. Shao, L. Jiao and Y. Deng, *Adv. Funct. Mater.*, 2025, **35**, e09656.
16 N. Thakur, Y. Ren, M. Kumar, T. Uchiyama, M. Fujita, I. Arima, M. Ishida, Y. Wu, Y. Tsuji, H. Imai, M. Matsumoto, Y. Zhuang, K. Yamamoto, T. Matsunaga, K. Ohara, M. Matsumoto, Y. Orikasa, Y. Kuroda, S. Mitsushima and Y. Uchimoto, *J. Am. Chem. Soc.*, 2025, **147**, 30613–30625.
17 T. Liu, Y. Wang and Y. Li, *Adv. Funct. Mater.*, 2022, **32**, 2207110.
18 Y. Wang, X. Bai, J. Huang, J. Zhang, W. Li, Y. Long, Y. Peng, J. Huang, H. Li, P. Tang and C. Xu, *ACS Catal.*, 2025, **15**, 17040–17053.
19 M. Yu, A. Li, E. Kan and C. Zhan, *ACS Catal.*, 2024, **14**, 6816–6826.
20 W. Li, Z. Guo, J. Yang, Y. Li, X. Sun, H. He, S. Li and J. Zhang, *Electrochem. Energy Rev.*, 2022, **5**, 9.
21 K. S. Exner, *Chem Catal.*, 2021, **1**, 258–271.
22 J. Pérez-Ramírez and N. López, *Nat. Catal.*, 2019, **2**, 971–976.
23 C. Brea and G. Hu, *J. Am. Chem. Soc.*, 2025, jacs.5c04776.
24 X. Li, X. Liu, M. Hussain, J. Li, Z. Chen, Y. Fang, C. Su, C. He and J. Lu, *ACS Nano*, 2025, **19**, 17114–17139.
25 X. Wu, Z. Yang, C. Li, S. Shao, G. Qin and X. Meng, *ACS Catal.*, 2025, **15**, 432–446.
26 C. Fang, J. Zhou, L. Zhang, W. Wan, Y. Ding and X. Sun, *Nat. Commun.*, 2023, **14**, 4449.
27 S. Huang, F. Lin, S. Wang, X. Zeng, H. Ling, X. Hu, Z. Shen and D. Cao, *Adv. Mater.*, 2024, **36**, 2407974.
28 J. Wang, X. Liu, C. Ma, X. Duan, S. Li, N. Li, W. Liu, Y. Li, X. Fan and W. Peng, *Adv. Funct. Mater.*, 2025, **35**, 2420157.
29 Y. Yin, L. Wang, H. Shang, X. Zhang, W. Chen and X. Zou, *ACS Nano*, 2025, **19**, 30338–30348.
30 L. Zhang, X. Guo, S. Zhang, T. Frauenheim and S. Huang, *Adv. Energy Mater.*, 2024, **14**, 2302754.

31 W. Chen, Z. Sun, S. Zhen, Y. Wang, J. Sun, M. Liu, W.-J. Han, L. Lai, W. Wei, L. Zhang and W. Chen, *Adv. Funct. Mater.*, 2025, **36**, e09200.
32 Y.-N. Gong, C.-Y. Cao, W.-J. Shi, J.-H. Zhang, J.-H. Deng, T.-B. Lu and D.-C. Zhong, *Angew. Chem., Int. Ed.*, 2022, **61**, e202215187.
33 L. Zhang, N. Zhang, H. Shang, Z. Sun, Z. Wei, J. Wang, Y. Lei, X. Wang, D. Wang, Y. Zhao, Z. Sun, F. Zhang, X. Xiang, B. Zhang and W. Chen, *Nat. Commun.*, 2024, **15**, 9440.
34 P. E. Blöchl, *Phys. Rev. B:Condens. Matter Mater. Phys.*, 1994, **50**, 17953–17979.
35 J. P. Perdew and A. Zunger, *Phys. Rev. B:Condens. Matter Mater. Phys.*, 1981, **23**, 5048–5079.
36 G. Kresse and J. Hafner, *Phys. Rev. B:Condens. Matter Mater. Phys.*, 1993, **47**, 558–561.
37 J. P. Perdew, K. Burke and M. Ernzerhof, *Phys. Rev. Lett.*, 1996, **77**, 3865–3868.
38 S. Grimme, S. Ehrlich and L. Goerigk, *J. Comput. Chem.*, 2011, **32**, 1456–1465.
39 H. J. Monkhorst and J. D. Pack, *Phys. Rev. B*, 1976, **13**, 5188–5192.
40 J. K. Nørskov, J. Rossmeisl, A. Logadottir, L. Lindqvist, J. R. Kitchin, T. Bligaard and H. Jónsson, *J. Phys. Chem. B*, 2004, **108**, 17886–17892.
41 V. Wang, N. Xu, J.-C. Liu, G. Tang and W.-T. Geng, *Comput. Phys. Commun.*, 2021, **267**, 108033.
42 R. F. W. Bader, *Chem. Rev.*, 1991, **91**, 893–928.
43 R. Nelson, C. Ertural, J. George, V. L. Deringer, G. Hautier and R. Dronskowski, *J. Comput. Chem.*, 2020, **41**, 1931–1940.
44 J. Fan, L. Yang and W. Zhu, *J. Mater. Chem. A*, 2024, **12**, 4258–4267.
45 Z. Zhang, X. Yang, K. Liu and R. Wang, *Adv. Sci.*, 2022, **9**, 2105201.
46 Y. Du, B. Xu, G. Wang, Y. Miao, B. Li, Z. Kong, Y. Dong, W. Wang and H. H. Radamson, *Nanomaterials*, 2022, **12**, 741.
47 J. Song, C. Wei, Z.-F. Huang, C. Liu, L. Zeng, X. Wang and Z. J. Xu, *Chem. Soc. Rev.*, 2020, **49**, 2196–2214.
48 L. Gao, X. Cui, C. D. Sewell, J. Li and Z. Lin, *Chem. Soc. Rev.*, 2021, **50**, 8428–8469.
49 W. Wan, Y. Zhao, S. Wei, C. A. Triana, J. Li, A. Arcifa, C. S. Allen, R. Cao and G. R. Patzke, *Nat. Commun.*, 2021, **12**, 5589.
50 I. Barlocco, L. A. Cipriano, G. Di Liberto and G. Pacchioni, *J. Catal.*, 2023, **417**, 351–359.
51 R. Shen, Y. Liu, S. Liu, J. Jiang, T. Liu, S. Mehdi, T.-H. Xiao, E. Liang and B. Li, *J. Energy Chem.*, 2025, **103**, 274–281.
52 G. Fu, W. Li, J.-Y. Zhang, M. Li, C. Li, N. Li, Q. He, S. Xi, D. Qi, J. L. MacManus-Driscoll, J. Cheng and K. H. Zhang, *Small*, 2021, **17**, 2006930.
53 L.-B. Liu, C. Yi, H.-C. Mi, S. L. Zhang, X.-Z. Fu, J.-L. Luo and S. Liu, *Electrochem. Energy Rev.*, 2024, **7**, 14.